Refraction effects of atmospheric inhomogeneities along the path

Arie N. de Jong

TNO-Physics and Electronics Laboratory, The Hague-Netherlands

ABSTRACT

A critical moment in the detection process of incoming targets at sea occurs, when a target just appears above the horizon. The corresponding light rays cross the atmospheric boundary layer, in which the presence of temperature gradients may result in optical distortion effects. This geometric distortion implies propagation effects such as the variation of the angle of arrival of the horizon line, a change in the shape of an extended target, the possible presence of mirages and enhanced or decreased atmospheric transmission or apparent radiant intensity of a point target. This situation is becoming even more complex, when the temperature profile is not constant over the path length, which is likely to be the case in coastal areas with tidal currents. Another effect causing complexity is the presence of surface waves, introducing vertical motion in the marine boundary layer. All these effects may have an impact on the detection performance of optical and infrared sensors for detection and identification of targets near the horizon. Presently available propagation models are unable to predict accurately the effect of the phenomena on the propagation of surface grazing light beams. A new and accurate ray-tracing model has been developed, allowing quantitative predictions of the various propagation effects for a given profile of the temperature. This model, capable to take into account the dimensions of the target and the receiver aperture, is described in the paper. The ray tracing in the model is based upon the Huygens-Fresnel principle, in contrary to other models, where a layered atmosphere is used. Examples are given of the effect of different temperature profiles and comparisons of predictions are made with data from field measurements.

Keywords: atmospheric propagation, refraction, transmission, IRST, point target detection, target identification

1. INTRODUCTION

Many publications have been written on refraction phenomena in images, obtained from celestial objects through a non-homogeneous atmosphere, for example recently on observations, made more than 400 years ago [1]. Lower to the earth surface, an everyday observable effect is the "water" above asphalt roads, heated by the sun during day-time. This "sky reflection" is actually due to refraction in a thin layer of air with a very strong negative temperature gradient in the first 10 cm above the asphalt. Even at sea, where the solar heating is much less, refractions may occur, as shown in Figure 1, where images of ships at the horizon appear very much distorted. As a result the probability of identification is strongly degraded. In the lower picture it is only possible to detect something hanging in the sky. Examples of distorted imagery over shallow water and sandbanks, are shown by Tränkle [2]. He introduces analytical temperature profiles, fitted to the observed phenomena. Similarly Lehn [3] is using a three parameter analytical expression for the temperature profile for explanation of inferior mirages of long distant mountains over an arctic sea. Several investigators (Vasilenko, Bruton, Young, Sampson and van der Werf) use the sun as target during sunset in order to obtain information on the temperature profile in the atmosphere [4,5,6,7,8].

A point target at low altitude is frequently seen as a pair of vertically separated point sources, because of the fact that in the marine boundary layer the air is cooler than the water. Due to the resulting negative temperature gradient, there are two possible light-paths from the source to the receiver. For each of the two paths the angle of arrival is different and in most cases the angular separation is more than a few tenths of a milliradian, sometimes just discernable with the unaided eye. This mirage effect for point targets has been investigated during several measurement campaigns. Forand reports about the MAPTIP trial in the North Sea [9], where a set of lamps was used at various altitudes above the water. Similar imagery was taken during the POLLEX trials in the Mediterranean Sea near Livorno over a range of 33 km [10] in the Baltic Sea near Stockholm over a range of 18 km [11] and near Kiel [12] and in the Pacific near Hawaii over a range of 16 km [13]. Figures 2, 3 and 4 show examples of refraction phenomena, observed during some of the latter trials.
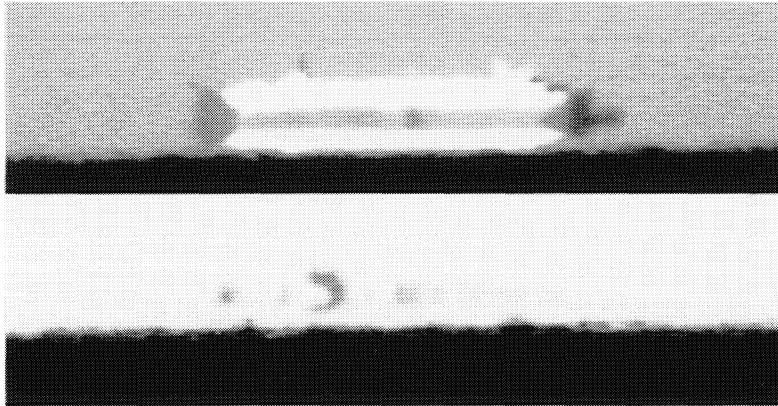
Figure 1. Examples of distorted images of ships near the horizon observed through a sub-refractive boundary layer. Images taken near Den Helder at the North-Sea coast on 9 January 2003 on a freezing day
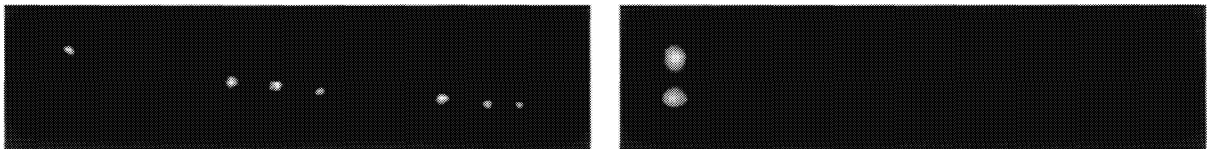

Figure 2. Images of an array of lamps at a distance of 18.5 km at various heights in the Baltic Sea 1999; left: super-refraction on 6 May, 19.20; all 7 lamps can be seen; right: sub-refraction on 8 May, 09.46; only one lamp is visible with its mirage; note the increased blur due to turbulence. Images taken with CCD camera from FOA-Sweden with 1.6 m focal length
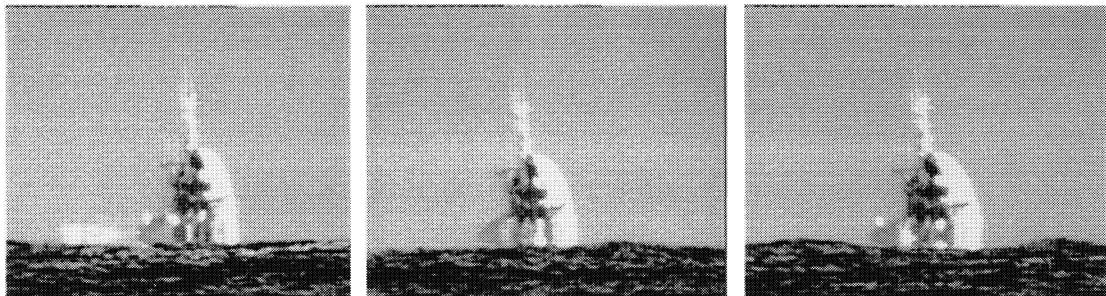

Figure 3. Images of one lamp at an altitude of 9.95 m, mounted on the "FLIP" near Hawaii at 16.4 km distance; 27 August 2001, 08.15 local time; camera height: 3.7 m, CCD camera with 1.25 m lens; effect is shown of slow moving waves, tilting the temperature profile during sub-refractive condition; images taken within 10 seconds.
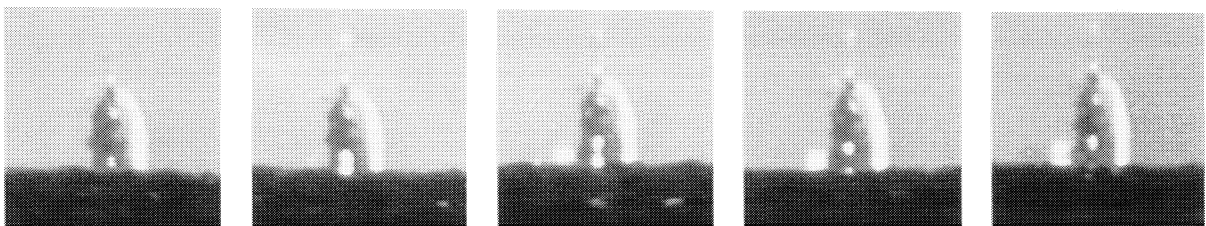

Figure 4. Images of the same lamp as in Figure 3; CCD camera with 400 mm lens at various heights; from left to right: 4.13 m, 4.52 m, 4.69 m, 4.87 m and 5.14 m above sea level; 4 September 2001, 07.45 local time

The pictures show long term or short term variations in the refraction phenomena due to a change in the weather, waves or sensor height variation. These variations may help to solve the inverse problem, another popular topic for investigators such as Fraser, Rees and Sozou [14,15,16]. It is very likely however, that the inversion of refraction data to temperature profile is impossible due to the fact that multiple profiles give similar effects. A standard temperature profile, used in many models follows from a micrometeorological bulk model of the marine boundary layer, which uses some basic parameters like the Air to Sea Temperature Difference (ASTD) and wind-speed [17]. The experiments show however that measured refraction effects do not correspond in many cases with the predicted ones. Apparently just one air temperature, measured at one specific height provides a too simple temperature profile. Many attempts have been undertaken to measure the profile in the boundary layer, for example with a balloon [18]. It is clear however that the profile, measured at one point in the path is not representative for the profiles over the total path length. Forand made a first attempt to take the variability of the profile along the path into account while validating this with the MAPTIP data [19].

As anomalous increase of the irradiance occurs when a point target pops-up over the horizon, enhanced detection probabilities are likely to occur [20]. Moreover very strong fluctuations are measured in this part of an incoming point target, as shown in [21]. In order to obtain more precise predictions of these measured effects, it was decided to develop a precision ray-tracing programme, capable to take into account temperature profiles based upon analytical functions, path inhomogeneities and layer tilting by waves. The programme has to provide a very precise calculation of the arrival height and angle of arrival as function of starting angle. One of the reasons to achieve high accuracy is the wish to obtain information of the sensitivity of output data on small changes in the profile input parameters. This information is of influence on the requirements concerning the accuracy of the meteorological parameters, measured during field experiments. With respect to this, one has to realize, that the performance of modern IR sensors can be very high, with NETD values of 20 mK, NEI's below 10 pW/m² and MTF's up to 10 c/mr. Visual camera's can easily provide a spatial resolution as low as 10 μr. The programme should therefore provide the distribution of intensity versus sensor height and angle of arrival, taking into account the size of the receiver pupil and the size of the source. Finally it is required to calculate the phase of the wavefronts arriving in a vertical plane at the receiver in view of the possibility of interference, which may influence the distribution of irradiance in the receiver plane and to scintillation in the case layers are fluctuating with time. In section 2 of the paper, details are presented on the ray-tracing programme. In section 3 examples are given of various output data, obtained with the programme. In section 4, measured data are compared with predictions and section 5 contains a discussion and conclusion.

2. THE RAY-TRACING PROGRAMME

The requirements for the new ray-tracing programme, as mentioned in the introduction, are summarized:
- Take into account the source dimensions and the receiver aperture
- Take into account layer tilting by water waves; amplitude and phase effects, resulting in low-frequency scintillation
- Take into account horizontal inhomogeneities of the temperature profile along the path
- Capability to adopt any analytical temperature profile
- Calculation of intensity profile versus sensor height and angle of arrival
- Calculation of intensity profile for variable ranges and source height
- Calculation of optical path-length differences with sub-micron accuracy
- The accuracy of the ray calculations in height should be better than 1 mm and 1μr in angle at 20 km range

The programme should of course provide the height at which a target can just be seen at a given range, or the range at which a target pops-up above the horizon.

Various methods for designing a ray-tracing programme have been published. Lehn [22] introduces a layered atmosphere, while applying Snell's law at each interface between two layers. This approach is not precise enough for our application. Other methods (like Claverie [23] and van der Werf [8]) are based upon solving the differential equations for propagation of a ray in a non-homogeneous atmosphere. The solution by numerical integration can in principle be done very accurate, although it is not easy to introduce inhomogeneities along the path. In the method, explained in this paper, a difference equation is set-up for any point O along the path, located at a height h_j above the undisturbed earth surface, while the slope of the ray makes an angle u_j with the local horizontal direction (see Figure 5).
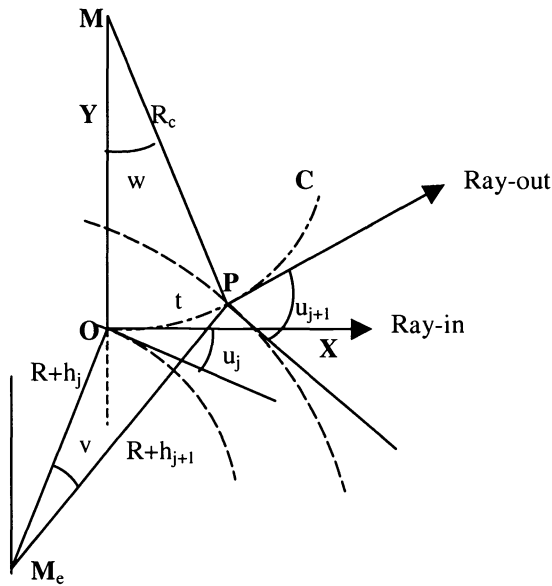
Figure 5. Illustration of geometry for ray-tracing calculations; **C** is circle of curvature; $\mathbf{M_e}$ is centre of earth; ray departs at **O** with j^{th} step and ends at **P** for starting $j+1^{th}$ step, running over a path-length of t, while the height above the earth surface increases from h_j to h_{j+1}

The distance of **O** to the centre of the earth $\mathbf{M_e}$ is $R+h_j$, where R stands for the radius of the earth. The calculation of the trajectory of the ray is done in steps; at point **O** the jth step is starting, where j is an integer number. During each step a new point **P** on the trajectory will be found, while a constant angular step v, considered from $\mathbf{M_e}$, is made. At the undisturbed earth surface the displacement is a constant path-length s = v*R. The first step in the calculation procedure is the determination of the average height p_j above the surface, taking into account a predefined wave structure, assuming that the atmospheric layer is tilted by the waves. At points **O** and **P**, the heights of the layer are q_j and q_{j+1}. The value of p_j is found by the approximation (1):

$$p_j = h_j + u_j * s / 2 + s^2 / 8R + (q_{j+1} - q_j) / 2 \tag{1}$$

The next step is the calculation of the ray curvature K_c at height p_j, which is determined by the gradient in the refractive index n at this height: $K_c = (dn/dh) / n$. When the value of K_c is positive, the ray curves upward with the centre of curvature in **M** and the radius of curvature $R_c = 1/K_c$ (see Figure 5). As the refractive index depends on the temperature T and pressure b, the profiles of n and dn/dh have to be converted to the profiles of T and b. Here the same approach will be taken as that by Lehn [22]:

$$n = 1 + (b / T) * 786 * 10^{-9} \quad and \quad dn/dh = - (dT/dh + 0.0348) * 786 * 10^{-9} * b / T^2 \tag{2}$$

For a barometric pressure of 10^5 N/m² and an air temperature of 290 K, equations (2) simplify into n = 1.000271 and:

$$dn/dh = - 9.35 * 10^{-7} * (dT/dh + 0.0348) \qquad (\text{in } m^{-1}) \tag{3}$$

Various T-profiles can be taken. One simple example is an exponential decrease or increase of temperature with height, combined with the adiabatic decrease of the temperature with height of 6 degree per km:

$$T (h) = (z / a) * \{exp(- a * h) -1\} - 0.006 * h \quad and \quad dT/dh = - z * exp(- a * h) - 0.006 \tag{4}$$

Where z and a are parameters, defining the slope of the temperature gradient and the ASTD. In order to incorporate the temperature inhomogeneity along the path, z and a are taken to be both a function of the step j. One example is a

sinusoidal variation of z and a with j:

$$z_j = z_0 - z_1 * \sin (2\pi j / N + \varphi) \quad \text{and} \quad a_j = a_0 - a_1 * \sin (2\pi j / N + \varphi) \tag{5}$$

where N and φ are constants, defining the number and phase of the periods over the total path-length. The next steps concern the calculations of h_{j+1} and u_{j+1}. With a very good approximation, as set by the required accuracy, the following relationships can be obtained:

$$h_{j+1} = h_j + s*[(1+ h_j)*v/2 + u_j*(1+ h_j / R + u_j^2/3) + s*(1+ h_j*2/R + u_j^2/2 + (u_j + s/2R_c)^2)/ 2R_c]+ q_{j+1} - q_j \tag{6}$$

$$u_{j+1} = u_j + v + s*[1 + h_j/ R + u_j^2 / 2 + v * u_j + (v + u_j) * s / 2Rc + (s / R_c)^2 / 6] / R_c \tag{7}$$

The final step concerns the calculation of the optical path-length over trajectory $t = w * R_c$ from **O** to **P**. In stead of taking the total path-length $n * t$, the difference $e = (n - 1) * t$ will be introduced, which becomes after some simplification:

$$e = s * 1.000271 * [- 9.35 * 10\text{-}7 * T (h) + h_j /R + u_j^2/2 + v* u_j + (v + u_j) * s / 2R_c + (s / R_c)^2 / 6] \tag{8}$$

where the temperature T (h) is taken at the average height p. The formula's (1) to (8) allow the complete ray tracing along any path-length required by taking the steps of j from j(0) to j(max). For the starting ray at j(0) one has to specify the starting height h(0) and angle u(0), where u is considered to be positive for positive elevation angles. At the receiver plane, located at a distance of $s * j(max)$, formula's (6) and (7) provide the arrival height h_a and arrival angle u_a. Via rather straightforward programming, one may easily calculate h_a and u_a as function of u(0) with h(0) as parameter. In this way atmospheric transfer characteristic functions are created, which directly give an indication of the refraction behaviour with a very high accuracy. It is interesting to trace the rays also back from the receiver plane to the target, as this gives information on the influence of h(0) on u_a at the pupil of a sensor.

Another task af the ray-tracing programme is the determination of the increase or decrease of irradiance due to refraction. It will be assumed that the refraction takes place only in the vertical direction (no horizontal gradients). In free space (no atmosphere), rays, departing in steps du, will arrive at the receiver plane at height differences $dh_a(fs)= s* j(max) * du$. In a refracting atmosphere the height differences dh_a tend to be dependent on the height of the receiver. The ratio $dh_a(fs)/dh_a = m$ provides the required change of irradiance, being a measure for the change in vertical ray density in the receiver plane. It is noted, that this ratio m is valid for a source with an infinitesimally small vertical size dh(0). For a source with a finite vertical size, ranging from height h(1) to h(2), one has to integrate m over this source height, while taking into account the height of the receiver pupil. Assuming, that all the light, collected at the entrance pupil of the receiver falls onto one detector, one has to count this amount. When a detector is used with high spatial resolution, the angle of arrival has to be taken into account, as the angle of arrival may vary over the entrance pupil. In this case the intensity may vary over the pixels. Example of this effect is shown in Figures 3 and 4. The equation for the magnification for the intensity M_i, as collected by a circular receiver pupil with diameter D_r, emitted by a circular source with diameter D_s, is found to be:

$$M_i = \int_{h_c(0)-D_s/2}^{h_c(0)+D_s/2} 4 * [\{D_s/2\}^2-\{h(0)-h_c(0)\}^2]^{0.5} * dh(0) \int_{h_a(c)-D_r/2}^{h_a(c)+D_r/2} m\{(h(0),h_a\} * [\{D_r/2\}^2-\{h_a-h_a(c)\}^2]^{0.5} * dh_a \tag{9}$$

in which $h_c(0)$ and $h_a(c)$ are the centre heights of the source and the receiver. In formula (9) the function m is effectively weighted over the source and receiver area. In this equation it is assumed, that no interference occurs in the receiver pupil area. This assumption will not be correct, when a number of rays are arriving with variable phase and approximately the same angle of arrival. This may happen in the case of sub-refraction at heights where mirages are observed. In this case the detected intensity pattern is more complicated. Formula (9) can be simplified in a number of cases, when m is not changing too much with h(0). The function m has nearly the same form for various heights h(0) values, shifted over a height $g * \{h(0)-h_c(0)\}$ in the receiver plane, where g is a magnification factor, depending on $h_c(0)$ and $h_a(c)$.

3. SAMPLE CALCULATIONS

The equations, governing the ray-tracing described in section 2, were written into a Quickbasic programme, which contains two FOR – NEXT loops, one for the steps i in the departing angle u and one for the steps j along the path. In this section some examples are presented on ray-tracing calculations for representative refractive conditions. First some standard ray tracings are given in Figure 6 for a sub-refractive and super-refractive condition with z = 0.5 (left) and - 0.5 (right). The value of a was 0.5 in both cases, which means that the 1/e value of the temperature drop occurs at a height of 2 m. The (point) source is located at a height $h_c(0)$ =10 m, and the receiver is located at a range of 25.6 km, while the sensor is estimated to be in the top of a mast of about 30 m. It is assumed that there are no waves, tilting the boundary layer and the atmosphere is homogeneous along the path. For the radius R of the earth the value of $6.37 * 10^6$ m has been taken. The graphs show that in the case of sub-refraction the sensor should be at least at a height of about 28 m to see the source, while for the case of super-refraction, the sensor is able to see the target even when he is located at sea level.
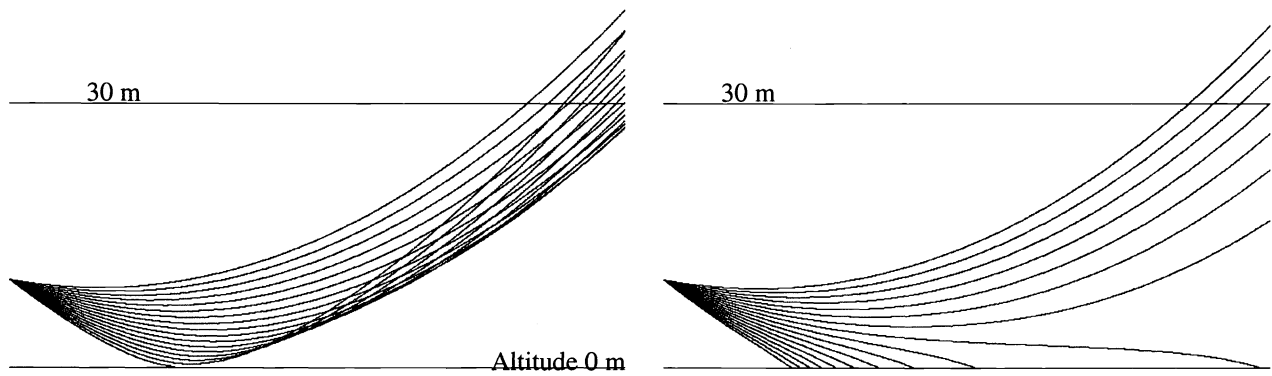

Figure 6. Standard ray-tracing with source at 10 m and receiver plane at 25.6 km range; left sub-refraction, ASTD = -1°C, right super-refraction, ASTD = +1°C; bundle of 17 rays, u(0) = - 0.0005, step = - 0.0001; the step size s is 10 m.

Figure 7 shows the behavior of the curvature along the 25.6 km path for the same sub-refractive atmosphere as shown in Figure 6, with an ASTD of –1 °C. The left plots are for the case of no surface waves; the right plots are for the case of water waves with an amplitude of 1 m and with a wavelength of 2000 m. The wavy plots show how the curvature changes along the path and the magnitude exceeds that of the left plots. The value of the curvatures up to 3*10-7 m-1 means a radius of curvature of more than 3000 km. One has to note the negative curvature for the first part and the latter part of the plots due to the decrease of atmospheric pressure with height.
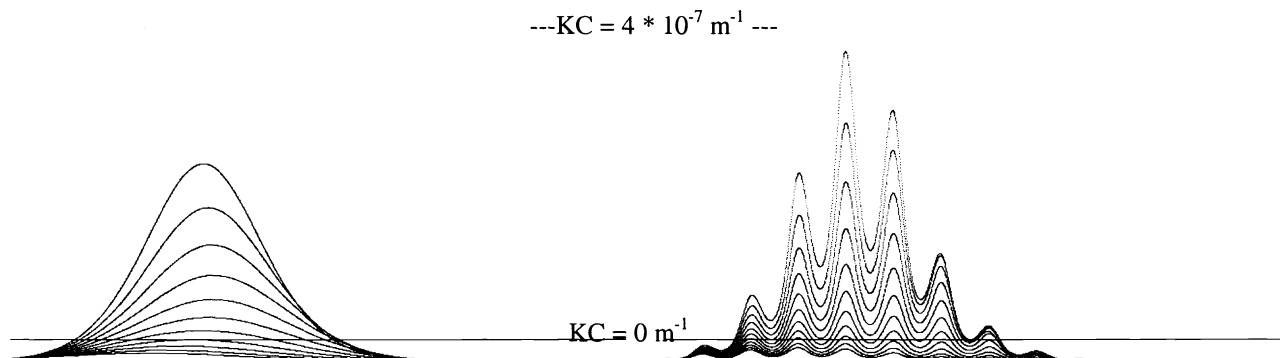
$$---KC = 4 * 10^{-7} \, m^{-1} ---$$

Figure 7. Plots of the curvature of the rays along the 25.6 km path. In both cases z and a have values of 0.5. The wave amplitude is 1 m. The rays departed at angles from u = -0.0008 in 10 steps of -0.0001 each

The next example is the behaviour of the optical path-length difference e over the path. Figure 8 shows two cases, one with a homogeneous atmosphere (left) and one with an atmosphere (right), in which the profile changes over the path according to formula (5). In this case z_0, z_1 and a_0 were all 0.5, while a1 and φ were both 0. For the number N a value of 1280 was chosen, which means that the period changes two complete cycles over the 25.6 km path. This period can be found back in the right plots of Figure 8. It is observed that e can obtain values of about 10^{-4} m, which takes place over a path step s of 10 m. It is noted that the phase difference for all rays are nearly the same at a range of about 4 km from the source. Apparently at this range all rays, with different departing angles, cross an area with the same gradient in refractive index for this kind of atmospheric profile.

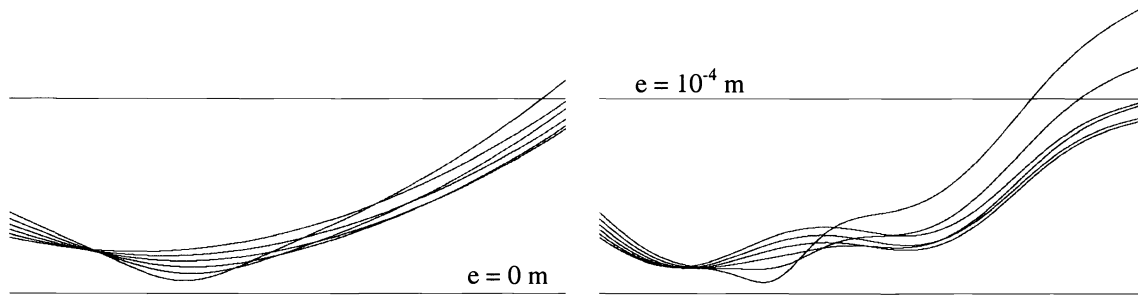$$e = 10^{-4} \text{ m}$$

$$e = 0 \text{ m}$$

Figure 8. Plots of optical path-length difference e per step j versus j for the whole path of 25.6 km; $z_0 = a_0 = 0.5$; left : homogeneous path; for the right picture $N = 1280$ and $z_1 = 0.5$; $s = 10$, $\varphi = 0$; $u(0) = -0.0008$, step -0.0002

Propagation Functions (FP's) are shown in Figure 9. The left picture shows plots of the arrival height versus departure angle for a homogeneous, sub-refractive atmosphere with $z = a = 0.5$ (ASTD = -1°C). For one arrival height two departure angles u are found, indicating the existence of a mirage. The right picture shows the super-refractive condition with $z = -0.5$ and $a = 0.5$ (ASTD = +1°C). Both pictures show the variation of the slope $s*j(max)*du/dh_a$ with arrival height h_a, indicating a variation of the ray density in the receiver plane. Compared to the free space slope, the ratio is higher for the sub-refractive case and lower for the super-refractive case. It is noted, that the curves for $h(0) = 9.8$ m and 10.2 m in the left picture have been shifted 20 μr to the right respectively left in order to show the minimum arrival height for the three departure heights $h(0)$ at about the same location. Similarly the curves have been shifted 10 μr to the left and right in the right picture for $h(0) = 9.8$ respectively 10.2 m. The curves show, that for different $h(0)$ values the shape of the FP remains about the same. The slopes of the three cases are however not identical, especially in the area of minimum h_a. At the location of the minimum in the left picture, the ray density goes to infinity. The curves show that the geometric magnification factor g in our example is 1.90.
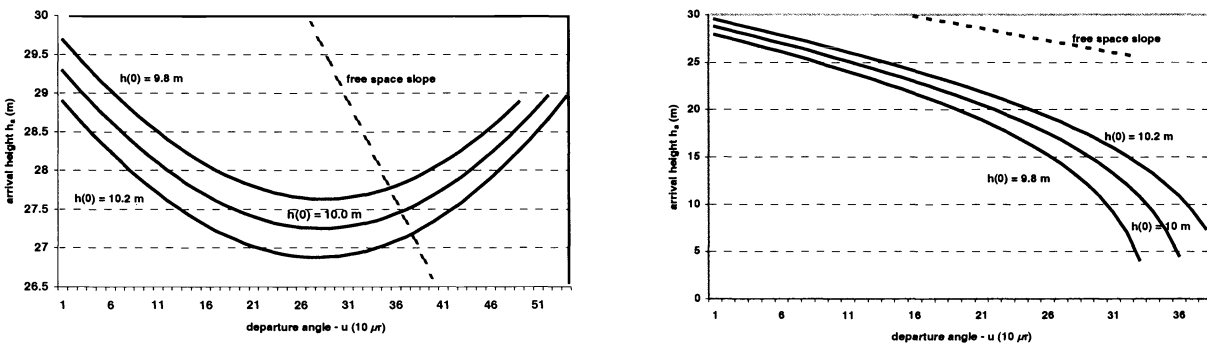
Figure 9. Propagation Functions FP for a sub-refractive (left) and super-refractive (right) atmosphere. The arrival height h is shown as function of the departure angle u for three source heights: 9.8 m, 10.0 m and 10.2 m For clarity the plots are shifted somewhat in horizontal direction

In Figure 10 in the left picture, typical model output is shown of the arrival angle u and the total optical path difference e as a function of the arrival height for the same sub-refractive conditions as before. For heights below 30 m two arrival angles are found, the higher corresponding to the mirage, separated about 0.3 mr from the real direction. The shape of the e-curve is approximately linear, which corresponds with the angles of the arriving rays. For example the ray, departing under an angle of $- 0.00117$ rad arrives at a height of 28.004 m with an arrival angle of 2.463 mr. For this angle an additional phase difference arises of 2.46 mm/m, while the real e difference is found to be 3.1 mm/m. This means that over a pupil with a size of 0.1 m, the phase of the wavefronts will vary 64 μm, which value is small enough to create interference effects. In the right picture it is shown that in the case of super-refraction, the source intensity is found to be less than 20% of the free space intensity for arrival heights below 10 m
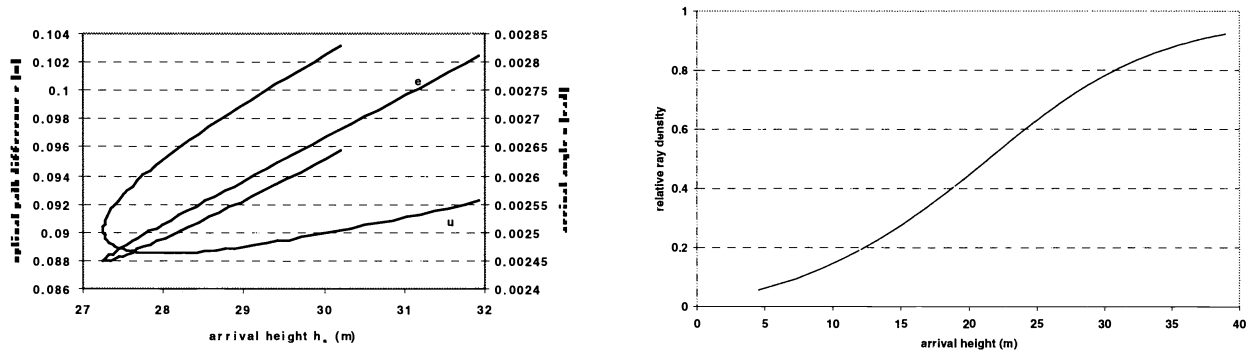

Figure 10. Model output for sub-refractive (e and u vs arrival height, left) and super-refractive (relative ray density, right) conditions, corresponding to Figure 9, $h(0) = 10$ m, $z_0 = -0.5$, $a_0 = 0.5$

Intensity increase occurs for the sub-refractive condition, following the function m in formula (9). If, for reasons of simplicity, interference effects are excluded, one can easily differentiate the Propagation Function in Figure 9 (left). The result is shown in Figure 11 (left). It is noted, that the ray density becomes very high at the minimum arrival height (note the log-scale). It is noted that when the sensor is placed one meter above the minumum arrival height (27.25 m), the ray density exceeds that of the free space condition with a factor 2.5 and 2.3 (for the mirage). If all rays are added, this would lead to a total m value of 4.8. For a sensor at 0.5 m above the minimum arrival height this factor would be 6.7. The right picture in Figure 11 shows the effect of the path inhomogeneity. In this case the following parameters in formula (5) were chosen: $z_0 = a_0 = 0.5$; $z_1 = 0.25$; $N = 5120$, while for φ values of 0, 1.57 and 3.14 were taken. It is clear that the position of the change in temperature profile along the path is of key importance to the propagation function. The shape of the functions, does not change so much, but their position is differing several meters in height.
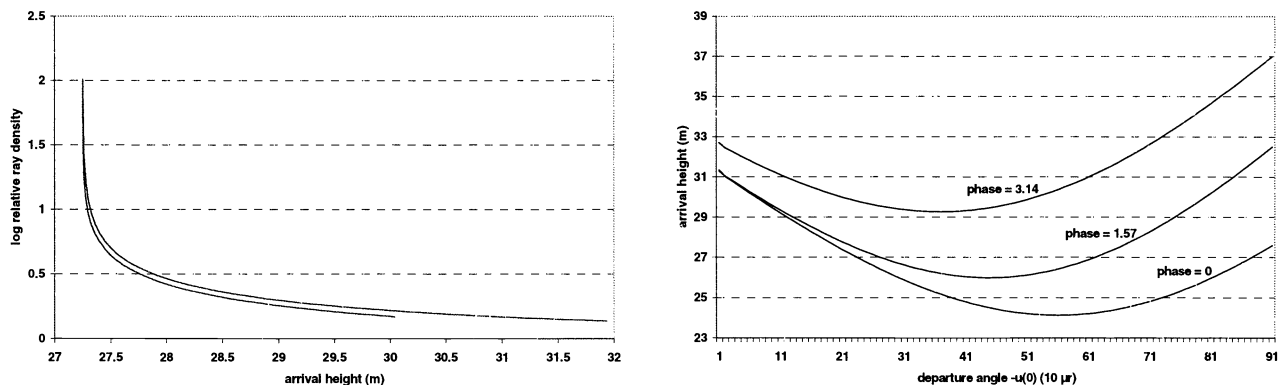

Figure 11. Relative ray density compared to free space condition for point target in sub-refractive condition ($h(0) = 10$ m) shown on log-scale (left). The right picture shows the effect of path inhomogeneity; the departure angle u(0) ranges from -0.0009, making steps of 10 μr

Another output from the model concerns the effect of the finite size of the source and the sensor. Of particular interest is the case of sub-refraction, where according to Figure 11 (left) the intensity rises to very high values for small sources and sensors. For the case of Figure 9 (left), with a source of 0.3 m high and a sensor (assumed here with a square pupil) with 0.1 m vertical height, the result of the integration process is shown in Figure 12 (left). For simplicity it was assumed that the shape of the Propagation Function was parabolic for the lowest part of the curve. The maximum intensity gain occurs near the minimum height for the central part of the source, and is reaching a value close to 6. This is for the single source, excluding the mirage; the mirage will have nearly the same intensity gain in this case. The right picture in Figure 12 shows the effect of wave-height on the minimum arrival height. In this case the source was again at 10 m height and at a range of 25.6 km. The wavelength of the surface waves L was 400 m. It is shown that small waves (<0.5 m) have very little effect on the minimum arrival height. It is noted that the rays, arriving at the minimum height, ar not approaching the sea surface closer than about 3 m; rays passing the surface at lower height, arrive much higher.
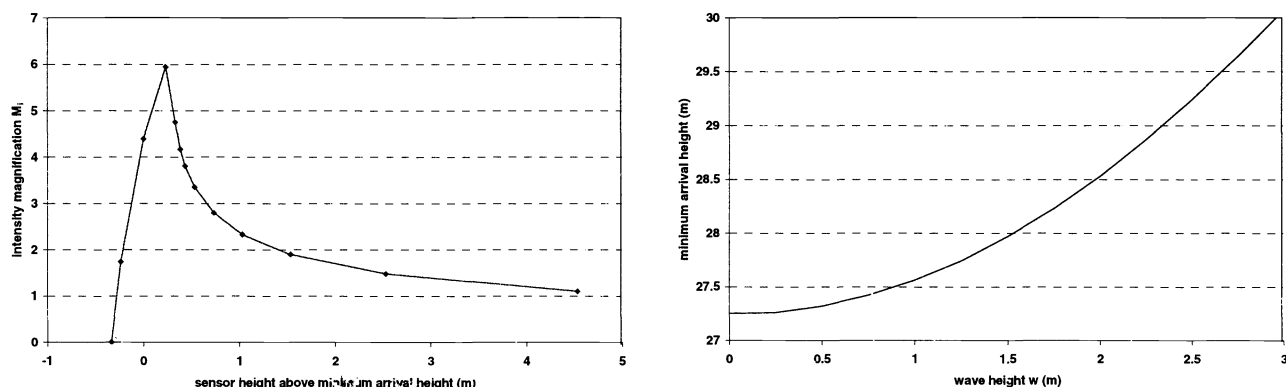

Figure 12. Intensity gain for finite source and sensor size (left); effect of wave height on minimum arrival height (right).

Finally some examples are given of the effect of the temperature profile. In Figure 13 (left), the propagation function is shown for the same ASTD values (-1°C), but different slopes of the profile. The difference in minimum arrival height is striking. In the case of $z_0 = a_0 = 2$, implying steeper slope in the profile, a target can be detected at about 10 m lower altitude; the intensity gain is generally less than in the case of $z_0 = a_0 = 0.5$. The target height is 10 m in both cases . The right picture shows the propagation functions for the profiles: $T(h) = 10/(30+h^3)$ and $T(h) = -(e^{-h}-1) + (e^{-0.5h}-1)$ as T-profiles 1 and 2. The FP in the first case shows a large horizontal area, resulting in a high local intensity. The second profile results in a situation of over the horizon viewing, while the rays with the largest negative departure angles are bending upward again.
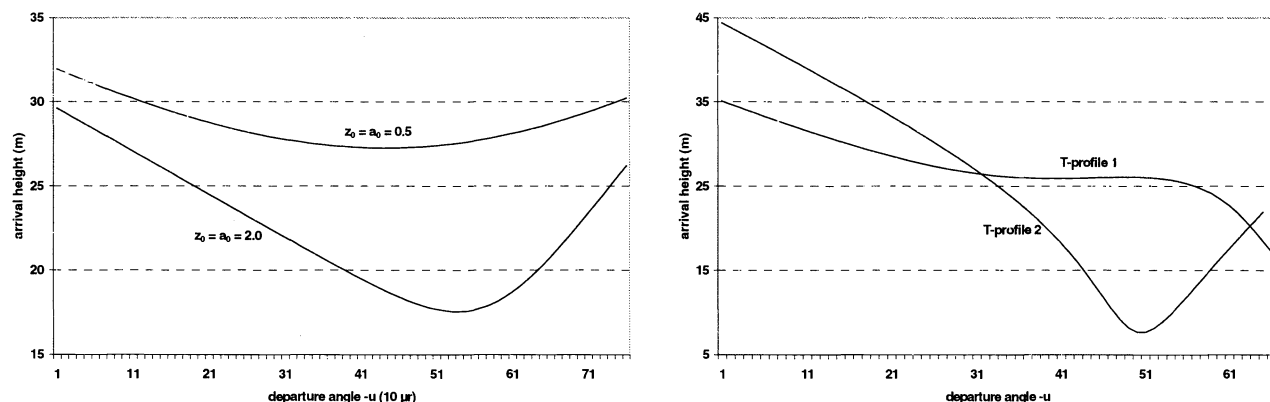

Figure 13. Effects of changes in temperature profile, left two sub-refractive conditions, both with ASTD = -1°C; right two different profiles, resulting in a kind of ducting condition. T-profile 1 has an ASTD of –0.33 °C at 0 m, while T-profile 2 has an ASTD of –0.25 °C at 1.5 m, returning to 0 °C at larger heights

4. MEASUREMENTS

Most of the images, taken of targets at long distance through an atmospheric boundary layer under refractive conditions, are difficult to interpret due to the lack of knowledge of the temperature profile along the path. On the contrary, it is difficult to predict the exact temperature profile, based upon the measured distortion. Distortions, such as shown in the Figures 1-4 may be produced by different profiles, moreover if the profile along the path is variable. In the case of sub-refraction, where just one point target is detectable together with its mirage, the image (or better image sequence) can basically provide the following information:

- angular distance between the real image of the point target and its mirage
- angular distance between the real image and the apparent horizon
- angular distance between the real image and the geometrical or real horizon
- ratio of the intensities of the real image and its mirage
- absolute intensity of both images (assuming the knowledge of the source intensity and the atmospheric extinction)
- size of the blurred spots of the real image and its mirage (in horizontal and vertical direction)

In this inverted process of the determination of the temperature profile from imagery, it is assumed that the position of the real horizon is known, as well as the sensor and target parameters. In view of the analysis of the intensity ratio, the signal should not saturate. In night-time or low-contrast conditions, the horizon may not be discernable in the images. It is noted that additional information can be collected by using cameras at various heights, while comparing the arrival angles as function of the arrival height. It is also noted, that the position of the mirage is most of the time located at the apparent horizon; this means, that, by moving the sensor up and down over a certain height difference h_d, making the mirage to appear and disappear, the value of h_d contains information on the temperature gradient in the boundary layer.

In the case of super-refraction, similar information can be obtained from the imagery. It is clear however, that more samples on the propagation function may be available, when an array of point sources is used, such as shown in the left picture of Figure 2. It is meaningful to invert the rays from the source to the sensor and to consider the departure angle as arrival angle for each of the sources with given height.
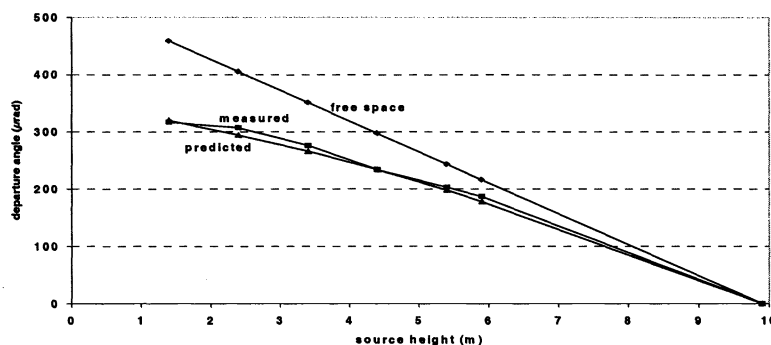

Figure 14. Comparison of measured and predicted apparent target height for the image of Figure 2 (left, Baltic May 1999)

In Figure 14 the result is shown of such an inverted calculation for the mentioned example. The straight line concerns the situation in free space (no refraction). The measured plot has been obtained from the picture, showing the typical super-refractive condition. For the predicted plot a profile according formulas (4) and (5) have been taken, whilethe following values for the parameters were taken: $z_0 = -0.08$; $z_1 = 0.05$; $a_0 = 0.7$; $a_1 = -0.1$; $N = 3700$; $s = 10$; $\varphi = 1.57$. The height of the sources were 9.9m, 5.9m, 5.4m, 4.4m, 3.4m, 2.4m and 1.4m. The receiver was located at a height of 9m at a range of 18.5 km. The departure angles were varied in steps of 10 μrad. The choice of the parameters implies a non-homogeneous profile over the path. If a homogeneous profile is taken, the predicted plot is curving too fast to the horizon. The predicted plot agrees quite well with the observation. It is however evident, that other profiles may produce the same or similar curves. It is noted, that the parameters chosen imply small positive ASTD's, as was the case, according to the data from a meteo buoy at a midpath location. The accuracy of these data was however not good enough for precise ray-tracing applications. It is also noted, that the air temperatures tend to change rapidly during the day.

This was also the case during the POLLEX trial in Livorno 2001 [10], of which some images are shown in Figure 15, taken in different conditions. The sources consisted of standard car head lights without glass, providing a collimated beam of about 2°. The heights of the sources above the sea level were: 51.0 m, 46.6 m, 42.6 m, 35.9 m, 33.0 m, 30.3 m, 24.2 m, 18.8 m and 12.4 m. Due to the variability in the weather conditions, both super-refractive (left and right picture) and sub-refractive (middle picture) propagation conditions did occur. In the case of super-refraction, all 9 sources were visible, while in the case of sub-refraction only the upper 6 sources were detectable including the mirages of the sources 5 and 6. The ASTD's (air temperature measured at 1 m height) measured at a mid-path buoy, were + 0.6 °C, 0 °C and 1 °C respectively (from left to right). It is noted, that in free space (no atmosphere), the camera would have detected just the upper 4 (close to 5) sources. It is also noted, that in the case of zero ASTD, pressure decrease with height causes always some super-refractive effect, resulting in the perceptability of the upper 6 sources (as low as 25.6 m).
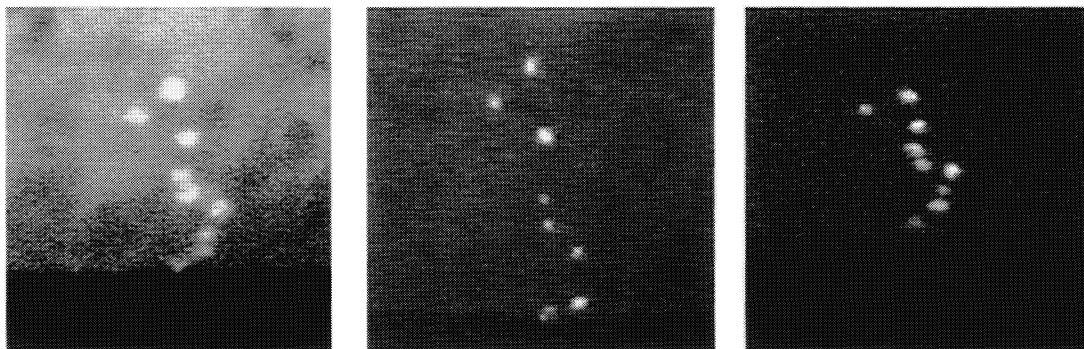

Figure 15. Examples of imagery, taken during the TG16 POLLEX trial, May 2001 in Livorno. From left to right: super-refraction on 10 May, 08.30, sub-refraction on 12 May, 07.50 and super-refraction on 17 May, 19.20. The images have been taken with a near-IR CCD camera with 1250 mm lens, giving a vertical FOV of 3.84 mrad. The 9 sources are located at a range of 34.2 km on Gorgona Island. The camera height was 14.5 m.

Similar to the previous example, the parameters of a temperature profile were determined, providing the best fit with the measured geometrical distortion. The results are shown in Table 1. It is shown, that the distortion on the 10th of May can be explained with a homogeneous atmosphere with constant profile, while on the 17th of May, the stronger distortion can only be explained with a variable profile. The distortion in the images on the 12th of May can not simply be explained with the standard profiles (4) and (5). The mirages appear however for the parameters, given in the table.

Table 1. Review of T-profile parameters, providing the best fit with distortion in POLLEX imagery (May 2001)

Date	z_0	z_1	a_0	a_1	φ
10 May	- 0.08		0.2		
12 May	0.24		1.45		
17 May	- 0.15	0.10	0.05	0.02	1.57

5. DISCUSSION

The ray-tracing scheme, presented in this paper, allows the investigation of the effect of atmospheric inhomogeneities along horizontal paths with variable temperature profiles. The methodology provides high precision output for arrival height, angle of arrival and phase at the receiver plane. The behaviour of the curvature of the rays along the path can be tracked, including in the case of tilting of the boundary layer by surface waves. Sample calculations are given of the

propagation function, defined by the relationship between arrival height and departure angle, and intensity as measured by the receiver for various atmospheric conditions. A comparison has been presented of measured and predicted propagation functions for the Baltic '99 and the POLLEX trials. It appears that generally the knowledge of the temperature profile based upon standard meteo equipment is highly inaccurate. The absolute apparent arrival angles for an array of point sources, provides a much more useful tool for the determination of the overall profile. If this is combined with an analysis of the measured absolute intensity of each souce by taking the slopes of the propagation function, even more information on the profile can be extracted. By analysing the blur, spot wander and intensity fluctuations (see also [21]), further information on the quality of image transfer by the atmosphere can be obtained.

REFERENCES

[1] Siebren Y. van der Werf et al, *Gerrit de Veer's true and perfect description of the Novaya Zemlya effect, 24-27 January 1597*, Applied Optics Vol. 42, No.3, 379-389, 20 January 2003

[2] Eberhardt Tränkle, *Simulation of inferior mirages observed at the Halligen Sea*, Applied Optics Vol.42, No. 9, 20 March 1998

[3] Waldemar H. Lehn et al, *A three-parameter inferior mirage model for optical sensing of surface layer temperature profiles*, IEEE Transactions on Geoscience and Remote Sensing, Vol. GE-24, No. 6, November 1986

[4] N. A. Vasilenko et al, *Determination of atmospheric temperature and pressure profiles from astronomical refraction measurements near the horizon*, Izvestia, Atmospheric and Ocean Physics, Vol. 22, No. 10, 1986

[5] William D. Bruton et al, *Unique temperature profiles for the atmosphere below an observer from sunset images*, Applied Optics, Vol. 36. No. 27, 20 September 1997

[6] Andrew T. Young et al, *Sunset science. II. A useful diagram*, Applied Optics, Vol. 37, No. 18, 20 June 1998

[7] Russel D. Sampson et al, *Comparison of modelled and observed astronomical refraction of the setting sun*, Applied Optics, Vol. 42, No. 3, 20 January 2003

[8] Siebren Y. van der Werf et al, *Novaya Zemlya effects and sunsets*, Applied Optics Vol. 42, No. 3, 20 January 2003

[9] J. Luc Forand, *MAPTIP: Refractive effects in the visible and IR*, SPIE Volume 2828, Image Propagation Through the Atmosphere, Denver, August 1996

[10] Arie N. de Jong et al, *TG16 point target detection experiment POLLEX, Livorno 2001*, SPIE Volume 4820, Infrared Technology and Applications XXVIII, Seattle, July 2002

[11] Arie N. de Jong et al, *Report on the Baltic 99 IR experiments*, TNO report FEL-00-A094, September 2000

[12] Karin Stein et al, *IR propagation through the marine boundary layer- comparison of model and experimental data*, SPIE Vol. 4884, International Symposium on Remote Sensing, September 2002, Crete

[13] Arie N. de Jong, *Visual and IR point detection experiments during RED, August-September 2001 in Hawaii*, TNO-report FEL-01-A311, January 2002

[14] Alistair B. Fraser, *Simple solution for obtaining a temperature profile from the inferior mirage*, Applied Optics Vol. 18, No. 11, 1 June 1979

[15] W. G. Rees et al, *Inversion of atmospheric refraction data*, J. Opt. Soc. Am. A, Vol. 8, No. 2, February 1991

[16] P. D. Sozou, *Inversion of mirage data: an optimisation approach*, j. Opt. Soc. Am. A, Vol. 11, No. 1, January 1994

[17] J. Luc Forand, *The L(W)WKD marine boundary layer model, version 7.09*, DREV Technical Report TR-1999-099, September 1999

[18] J. Ross Rottier et al, *APL environmental assessment for Navy Anti-Air Warfare*, Johns Hopkins APL Technical Digest, Vol. 22, No. 4 (2001)

[19] J. Luc Forand, *Horizontal non-homogeneous effects in the marine boundary layer*, SPIE Volume 3125, Propagation and Imaging through the Atmosphere, San Diego, July 1997

[20] Arie N. de Jong et al, *Enhanced IR point target detection by atmospheric effects*, SPIE Volume 4820, Infrared Technology and Applications, Seattle, July 2002

[21] Arie N. de Jong, *Intensity variations of small airborne incoming targets, popping-up above the horizon*, SPIE Vol. 5237, Optics in Atmospheric Propagation and Adaptive Systems VI, Barcelona, September 2003

[22] Waldemar H. Lehn, *A simple parabolic model for the optics of the atmospheric surface layer*, Appl. Math. Modelling, Vol. 9, December 1985

[23] Jacques Claverie et al, *Modelling optical refraction and turbulence effects with the MSBL*, SPIE Vol. 4167, Atmospheric Propagation, Adaptive Systems and Laser Radar Technology, Barcelona, September 2000